Journal of Fluids Engineering

Technical Briefs

# An Experimental Investigation of the Effect of Freestream Turbulence on the Wake of a Separated Low-Pressure Turbine Blade at Low Reynolds Numbers

**C. G. Murawaski**
Research Engineer, Propulsion Directorate, AFRL/PRTT, Bldg 18, 1950 Fifth Street, WPAFB, OH 45433-7251

**K. Vafai**
Professor, Ohio State University, Department of Mechanical Engineering, 206 W. 18th Avenue, Columbus, OH 43210-1107; Fellow ASME

*An experimental study was conducted in a two-dimensional linear cascade, focusing on the suction surface of a low pressure turbine blade. Flow Reynolds numbers, based on exit velocity and suction length, have been varied from 50,000 to 300,000. The freestream turbulence intensity was varied from 1.1 to 8.1 percent. Separation was observed at all test Reynolds numbers. Increasing the flow Reynolds number, without changing freestream turbulence, resulted in a rearward movement of the onset of separation and shrinkage of the separation zone. Increasing the freestream turbulence intensity, without changing Reynolds number, resulted in shrinkage of the separation region on the suction surface. The influences on the blade's wake from altering freestream turbulence and Reynolds number are also documented. It is shown that width of the wake and velocity defect rise with a decrease in either turbulence level or chord Reynolds number.*
[S0098-2202(00)00202-9]

## Introduction

For low-pressure turbines at low Reynolds numbers, the laminar boundary layer in the aft portion of the suction surface can be susceptible to large unsteady flow separation. This results in a degradation of overall turbine engine performance (Sharma et al. [1]). For this reason, low-pressure turbine aerodynamics has received an increased level of attention recently. Research conducted by Baughn et al. [2], Qui and Simon [3], and Bons et al. [4] have shown that profile losses increase as the Reynolds number decrease due to flow separation on the suction surface.

An experimental study was conducted in a two-dimensional linear cascade with low-pressure turbine blades. Flow Reynolds numbers, based on exit velocity and suction surface length, were varied from 50,000 to 200,000. Freestream turbulence was varied from 1.1 to 8.1 percent. Parts of the results in this report were presented in Murawski et al. [5]. The results are revisited and updated, focusing on Reynolds number and turbulence level effects on a low-pressure turbine airfoil and documenting the effect of these influences on the airfoil wake.

**Experimental Apparatus.** Figure 1 shows a schematic of the test apparatus. A centrifugal blower, controlled by a variable speed motor controller, pulls air through the apparatus. The inlet freestream turbulence intensity can be elevated by a passive turbulence grid located 1.45 m upstream of the cascade row. The grid is a wooden square mesh of 13 mm square bars with a 25.4 mm center-to-center spacing.

The cascade contains four low-pressure turbine blades with an axial chord length of 10.36 cm and a span-to-chord length aspect ratio of 1.1. The suction surface length is 15.24 cm. The pitch-to-chord ratio (solidity) is 0.88 and the flow is turned through 95 deg.

Instantaneous local velocities were acquired using a single element, hot-film probe. Mean upstream velocity and total pressure measurements were acquired with a pitot-static probe. Surface static pressures were measured using static pressure ports located at midspan on the surface of one blade.

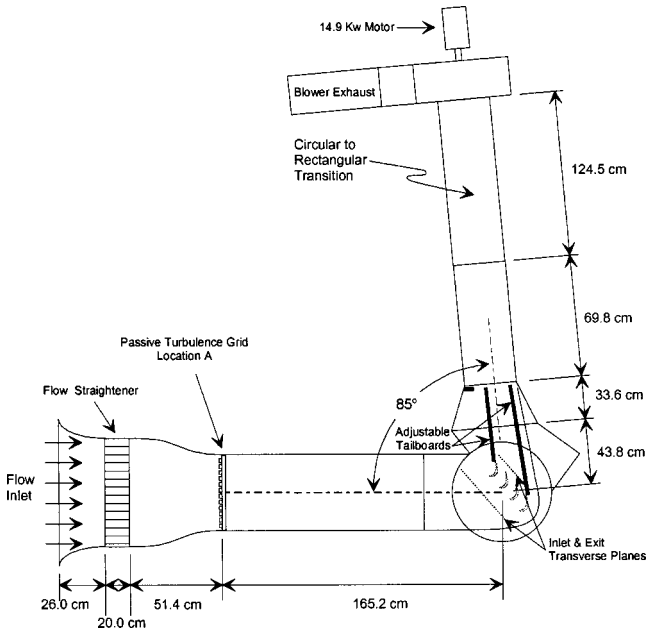


**Fig. 1 Test apparatus schematic**

Contributed by the Fluids Engineering Division of THE AMERICAN SOCIETY OF MECHANICAL ENGINEERS. Manuscript received by the Fluids Engineering Division March 3, 1999; revised manuscript received December 20, 1999. Associate Technical Editor: P. E. Raad.

  

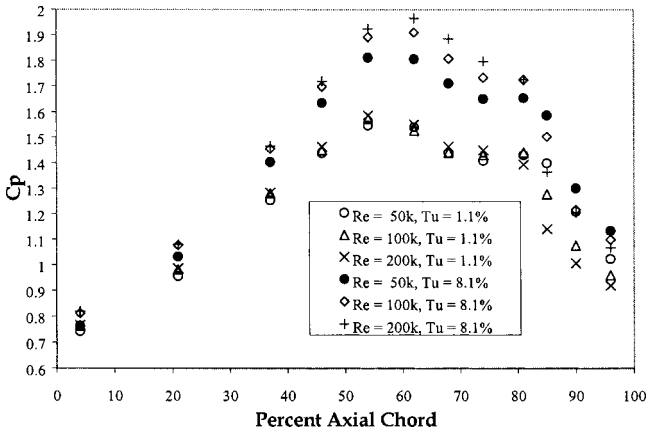


**Fig. 2 Surface static pressure survey**

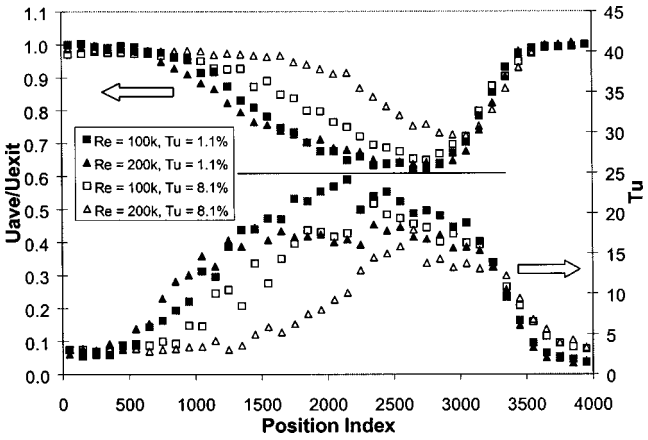


**Fig. 4 Wake velocity survey for the average velocity and turbulence intensity**

The experimental uncertainties were established using the method of Kline and McClintock [6]. The uncertainty of the velocity measurements from the pressure transducers and the single wire, hot-film probe was less than 2 percent. The maximum uncertainty in the pressure coefficient measurement was less than 4 percent.

## Results

**Inlet Profile.** An inlet profile survey was performed by measuring velocities using a single hot-film probe located one blade chord upstream of the leading edges at mid-tunnel height. Without a turbulence generation grid, the inlet flow turbulence intensity was 1.1 percent. The passive turbulence grid created an inlet freestream turbulence level of 8.1 percent. The inlet axial flow velocity was uniform to within 7.5 percent with and without the turbulence grid.

**Surface Static Pressure Results.** Surface static pressure surveys for the suction surface of the turbine blade with freestream turbulence levels of 1.1 percent and 8.1 percent are presented in Fig. 2 in terms of a pressure coefficient defined by:

$$C_p = \frac{(P_{T\,\mathrm{in}} - P_{Si})}{\frac{1}{2}\rho U_{\mathrm{exit}}^2} \tag{1}$$

Along the suction side surface, from 0 to 50 percent of axial chord, the boundary layer remains attached for all Reynolds numbers. Over the last 50 percent of the suction side surface the boundary layer is affected by changes in Reynolds number and freestream turbulence intensity.

The pressure coefficient profiles of Fig. 2 contain a terrace (flat zone) in this region. Gaster [7] explained that the terrace is created by the initial portion of the separation bubble composed of a laminar shear layer and a dead air region. The shear layer then begins to interact with the separation bubble. A region of turbulent mixing occurs which may result in boundary layer reattachment. At the end of the dead air zone the magnitude of the velocity will increase near the wall. The initiation of transition appears as a region on the pressure coefficient curve that quickly falls off after the flat zone.

A separation zone is present in the pressure coefficient profiles for all Reynolds numbers. Increasing the Reynolds number results in a smaller terrace, which indicates a reduced size of the separation zone. Increasing both Reynolds number and freestream turbulence results in a smaller separation zone. The exact location of separation, transition, and reattachment are not precisely ascertained from surface static pressure surveys. However, the trends of Fig. 2 are consistent with and add value to the observations in the following sections.

**Wakes.** Changes in the size, length, and location of the separation zones on the turbine blade influence the size and strength of the wake. Each point on Fig. 3 represents a local instantaneous velocity recorded while a hot film probe was traversed parallel to and 2.54 cm behind the plane of the trailing edges of the cascade

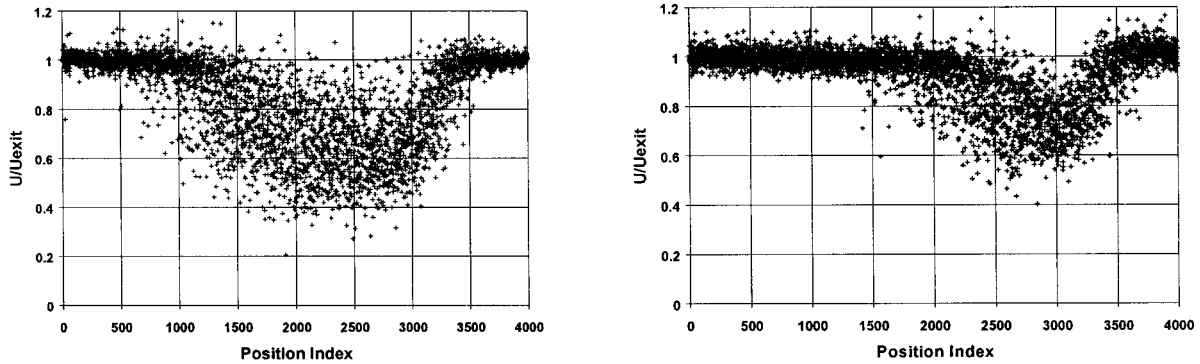


(a) Re =100k, Tu = 1.1%

(b) Re = 200k, Tu = 8.8%

**Fig. 3 Instantaneous velocity wake survey: (*a*) Re=100 k,Tu=1.1 percent, (*b*) Re=200 k,Tu=8.1 percent,**

turbine blade. Figure 3 shows that the wake dramatically decreases in size when the Reynolds number is increased from 100,000 to 200,000 and the freestream turbulence increases from 1.1 percent to 8.1 percent.

Figure 4 provides spatial averages of the instantaneous velocity surveys in the wake of the turbine blade wake. Spatial averages of velocity and turbulence intensity were calculated by averaging every 100 data points. The largest velocity defect and largest spatial turbulence intensity occurs when the freestream turbulence is 1.1 percent. At the lower Reynolds numbers, the thicker boundary layer, caused by flow separation at the rear of the suction surface, creates a larger local pressure drop, and more mixing occurs in the shear layer between the detached boundary layer and the freestream. This creates a larger wake and thus increased profile loss from the blade. As the Reynolds number is increased, with a freestream turbulence level of 1.1 percent, the level of fluctuation is diminished, while the width of the wake is almost constant.

Increasing the freestream turbulence level to 8.1 percent has a profound effect on the separation region on the suction side of the turbine blades in this cascade configuration. In each case, when the Reynolds number was kept constant and the freestream turbulence level was increased, the magnitude of the velocity deficit and the width of the wake decreased. The increase in freestream turbulence level diminishes the size of the separation region resulting in lower profile losses. In Fig. 4, when the freestream turbulence is held constant at 8.1 percent and the Reynolds number is increased, the velocity deficit and wake width decrease because the size of the separation zone is decreasing.

## Conclusions

The effect of Reynolds number and freestream turbulence intensity on a low-pressure turbine cascade blade has been investigated in this work. The condition of the blade's boundary layer was the leading factor in the level of losses recorded in the wake. The losses from the blade decreased as the Reynolds number and freestream turbulence were increased.

At low levels of freestream turbulence, increasing the Reynolds number reduced the velocity deficit in the wakes, but did not reduce the width of the wake, resulting in only a minimal reduction of the profile losses.

For cases of freestream turbulence intensity of 8.1 percent, as Reynolds number increased, the suction side boundary layer changed dramatically. With increasing Reynolds number, the separation zone became smaller, reducing the velocity defect and decreasing the wake width, resulting in a substantial reduction in the blade's profile losses.


## Acknowledgments

The assistance of Dr. Richard Rivir and Dr. Rolf Sondergaard of the Air Force Research Laboratory Propulsion Directorate is acknowledged. Professor Terrence Simon of the University of Minnesota and Dr. Ralph Volino of the U.S. Naval Academy provided technical support. The authors are grateful to Dr. Paul King of the Air Force Institute of Technology for use of the linear cascade.


## Nomenclature

- $Cp$ = local pressure coefficient
- $P_{Si}$ = static pressure along the blade surface
- $P_{T\,\mathrm{in}}$ = total pressure at inlet to blade set
- Tu = freestream turbulence intensity ($u'_{\mathrm{rms}}/\overline{u}_{\mathrm{local}}$)
- $U_{\mathrm{exit}}$ = velocity at the exit of the blade set
- $\overline{u'}_{\mathrm{rms}}$ = root mean square of the fluctuating component of streamwise velocity
- $\overline{u}_{\mathrm{local}}$ = local mean streamwise velocity
- $\rho$ = density

## References


[1] Sharma, O. P., Ni, R. H., and Tanrikut, S., 1994, ''Unsteady Flows in Turbines-Impact on Design Procedure,'' AGARD-LS-195, Paper No. 5.

[2] Baughn, J. W., Butler, R. J., Byerley, A. R., and Rivir, R. B., 1995, ''An Experimental Investigation of Heat Transfer, Transition and Separation on Turbine Blades at Low Reynolds Number and High Turbulence Intensity,'' ASME Paper No. 95-WA/HT-25.

[3] Qiu, S., and Simon, T. W., 1997, ''An Experimental Investigation of Transition as Applied to Low Pressure Turbine Suction Surface Flows,'' ASME Paper No. 97-GT-455.

[4] Bons, J. P., Sondergaard, R., and Rivir, R. B., 1999, ''Control of Low-Pressure Turbine Separation Using Vortex Generator Jets,'' AIAA Paper No. 99-0367.

[5] Murawski, C. G., Sondergaard, R., Rivir, R. B., Vafai, K., Simon, T. W., and Volino, R. J., 1997, ''Experimental Study of the Unsteady Aerodynamics in a Linear Cascade with Low Reynolds Number Low Pressure Turbine Blades,'' ASME Paper No. 97-GT-95.

[6] Kline, S. J., and McClintock, F. A., 1953, ''Describing Uncertainties in Single-Sample Experiments,'' Mechanical Engineering, **75**, pp. 3–8.

[7] Gaster, M., 1966, ''The Structure and Behavior of Laminar Separation Bubbles,'' AGARD-CP-4, pp. 819–854.


# Experimental Investigation of Flow Through an Asymmetric Plane Diffuser

## (Data Bank Contribution)[1]


**Carl U. Buice**
Director of Application, Genemachines,
San Carlos, CA 94070

**John K. Eaton**
Department of Mechanical Engineering, Stanford University, Stanford, CA 94305
e-mail: eaton@vk.stanford.edu



[S0098-2202(00)00302-3]


## Introduction

This data bank contribution provides measurements for a two-dimensional diffuser flow which includes separation and reattachment forming a separation bubble on one wall of the diffuser. Separated flows are difficult to predict because the separating and reattaching boundary layers are highly out of equilibrium. Advanced simulation techniques including large eddy simulation and detached eddy simulation are being developed to compute separated flows. Such simulations require realistic, time-dependent inflow conditions. These are most easily generated if the inlet flow is simple. For this reason, Obi et al. [1] made measurements in a nominally two-dimensional separated diffuser flow with fully developed channel flow inlet conditions. The test case is widely used, but there are questions about the two dimensionality of the flow.

The objective of the present work was to repeat the Obi et al. experiment using a larger aspect ratio apparatus and paying extra attention to the treatment of the endwall boundary layers. In addition, the straight tailpipe section of the diffuser was extended to allow a more extensive examination of the boundary layer down-

[1]Data have been deposited to the JFE Data Bank. To access the file for this paper, see instructions on p. 463 of this issue.


Contributed by the Fluids Engineering Division of THE AMERICAN SOCIETY OF MECHANICAL ENGINEERS. Manuscript received by the Fluids Engineering Division July 7, 1999; revised manuscript received January 25, 2000. Associate Technical Editor: D. P. Telionis.

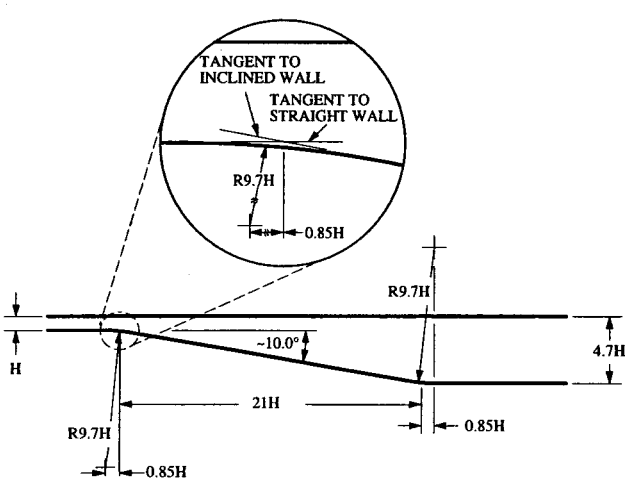


**Fig. 1 Detailed drawing of test section geometry**

stream of reattachment. This is an especially useful case for the study of recovering flows because the flow has a known end state of fully developed channel flow.

## Experimental Apparatus and Techniques

The experiments were conducted in the blower-driven wind tunnel of Anderson and Eaton [2] modified with an additional contraction to a two-dimensional, plane-wall channel flow with a channel height H of 15 mm and a width of 610 mm. The high aspect ratio (41:1) inlet channel is 1.65 m long providing ample length to obtain fully developed turbulent channel flow at the inlet of the diffuser test section. The diffuser geometry shown in Fig. 1 replicates the geometry of Obi et al. [1]. There is an asymmetric expansion with an area ratio of 4.7 over a distance of 21 H giving a diffuser angle of 10 degrees. The rectangular tailpipe section (70.5 mm×610 mm) extends 56 H downstream of the diffuser before the flow exits to the room through a grid.

Even with the large aspect ratio, special care was required to obtain a two-dimensional flow. The endwall boundary layers were removed by adding thin splitter plates 4.7 H from each end wall starting 6 H upstream of the diffuser and extending to the end of the tunnel. A row of small holes was drilled through the splitter plates 3 H downstream of the diffuser inlet to thin the new end-wall boundary layer. Suction in the end-wall sections was adjusted to obtain two-dimensional flow everywhere in the test section. Buice and Eaton [3] document numerous tests of the two-dimensionality including measurements of the spanwise uniformity of the mean velocity and skin friction, and calculated balances of mass and momentum. The tests show that the flow is two dimensional to within the measurement resolution.

Multiple probe systems were used to provide the best accuracy in each region of the flow and to provide redundant measurements where possible. Wall static pressure was measured using 0.64 mm diameter taps connected to a Celesco P7D pressure transducer (+/−0.1 psid range). Overall uncertainty was less that 0.001 in. of water.

Mean velocity and turbulent stresses were measured using hot-wire anemometry in regions where the streamwise turbulence intensity was less than 30 percent. Details of the probes and techniques are given in Buice and Eaton [3]. The techniques were similar to those reported in Anderson and Eaton [1]. Single-wire measurements had mean velocity uncertainty of 2 percent and streamwise turbulence intensity uncertainty of 4 percent, except near the wall in the upstream channel as discussed below. Cross-wire uncertainty was 5 percent for the wall-normal Reynolds stress, and 10 percent for the shear stress, $u'v'$. Redundant measurements of the mean velocity and streamwise normal stress agreed with the single-wire results within the uncertainty estimates.

A single component pulsed wire anemometer was used for velocity measurements in the highly turbulent separated shear layer and in the recirculation zone. The mean velocity uncertainty was estimated to be 2 percent for velocities ranging from 5 to 12 m/s and around 5 percent for lower velocities. The uncertainty in the measurement of $u'$ was less than 5 percent in regions of high

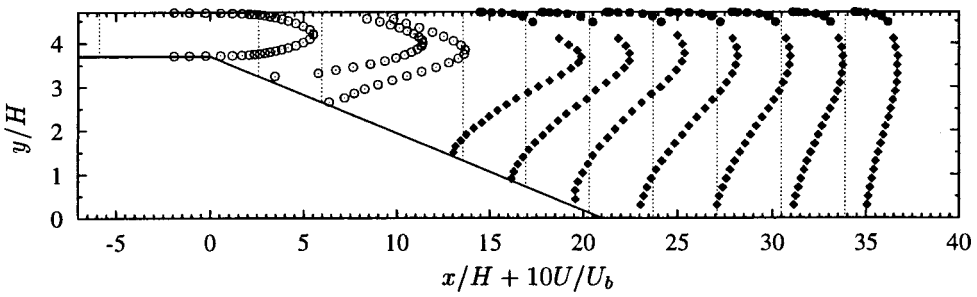


**Fig. 2 Mean velocity profiles, $U/U_b$: ○, single wire boundary layer probe; ◇, pulsed wire probe; ●, single wire wall probe**

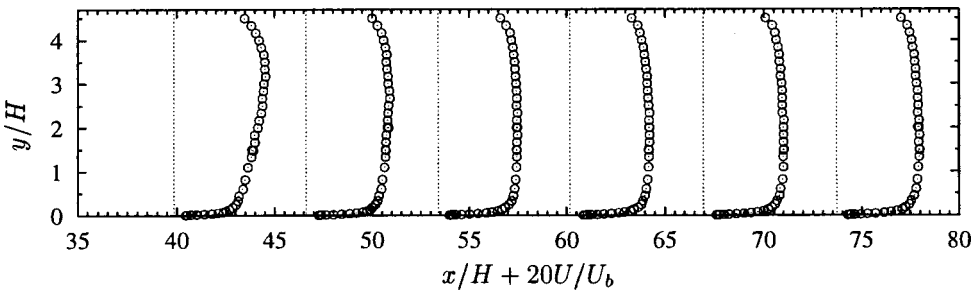


**Fig. 3 Mean velocity profiles, $U/U_b$: ○, single wire boundary layer probe**

turbulence intensity ($u'/U > 0.05$). In regions of lower turbulence intensity, the pulsed-wire turbulence measurements are unreliable, and we present only hotwire results.

A special wall mounted pulsed-wire called the pulsed-wall probe (Westphal et al. [4]) was used to measure near-wall velocity profiles in the recirculation region, and to infer the wall shear stress by moving the measurement location very close to the wall. With the wire drawn into the nearest position ($y = 0.15$ mm) the probe was calibrated directly for skin friction using fully developed channel flow as a reference. The uncertainty in the skin friction measurements was estimated to be a constant 0.02 N/m$^2$.

### Data Reported in the Archive

All data in the archive are presented in a coordinate system in which the $x$-axis is parallel to the upstream channel, and has its origin at the intersection of the two lines tangent to the inlet channel wall and the inclined wall. The $y$ axis is normal to the $x$ axis and thus to the undeflected wall of the diffuser. The origin of the $y$ axis is on the lower wall of the tailpipe so all $y$ values are positive. All distances are normalized by the height of the inlet channel, $H$. Velocities are normalized by the bulk average velocity in the upstream channel, $U_b$. The upstream channel centerline velocity is $1.14U_b$. The tunnel was operated at $U_b = 20$ m/s giving an inlet channel Reynolds number, $U_bH/\nu$ of 20,000.

In comparing to the present data set, it is important that computations of the flow begin some distance upstream of the diffuser inlet since the streamlines begin to curve upstream of $x = 0$, causing local acceleration and distortion of the velocity profile. For this reason, the inlet conditions are specified at $x/H = -5.1$ where pressure measurements indicate a constant pressure gradient characteristic of fully developed channel flow. The present mean velocity and turbulence profiles are in excellent agreement with the data of Hussain and Reynolds [5], measured at a channel height Reynolds number of 21,300. The only exception are the turbulence intensity measurements for $y/H < 0.025$ where the present measurements are 10 to 20 percent lower. This is due to the inadequate spatial resolution of the single-wire probe which was 0.6 mm (45 wall units) long. The mean velocity and turbulence data indicate that the inlet flow has the characteristics of fully developed channel flow, and that any well-qualified channel-flow simulation can be used to provide inlet conditions for the diffuser simulation.

Figures 2 and 3 show the mean velocity profiles, illustrating the distribution of profile locations and the general development of the flow. Streamwise turbulence intensity, wall normal stress, and the Reynolds shear stress were all measured at the same profile locations. Note that the wall normal stress and Reynolds shear stress profiles do not extend into the separated flow region, where the cross wire would have a very large uncertainty. In addition to these profiles, measurements of the static pressure and the skin friction along the entire length of both test section walls are included in the data set. This includes measurements in the separated flow region where the pulsed-wall probe supplied measurements of the reverse-flow skin friction.

There are two aspects of this data set that offer a particular challenge to model developers. First, is the smooth wall separation and reattachment that make this case more challenging than the backward-facing step and similar abruptly separated flows. Also, of great interest is the recovering channel flow in the tailpipe. The profile near the wall recovers until it is virtually identical to the upstream channel. On the other hand, the velocity is more uniform than developed channel flow in the central region due to the strong turbulent mixing produced by eddies remaining from the separated flow. Thus, the turbulence is far from equilibrium with the mean flow, and offers a good test for length scale transport equations. The thermal diffusivity in this region is also far out of equilibrium, as shown by Buice and Eaton [6].

### References


[1] Obi, S., Aoki, K., and Masuda, S., 1993, ''Experimental and Computational Study of Separating Flow in an Asymmetric Planar Diffuser,'' *9th Symposium on Turbulent Shear Flows*, Kyoto, Japan, pp. 305-1–305-4.

[2] Anderson, S. D., and Eaton, J. K., 1989, ''Reynolds Stress Development in Pressure-Driven Three-Dimensional Turbulent Boundary Layers,'' J. Fluid Mech., **202**, pp. 263–294.

[3] Buice, C. U., and Eaton, J. K., 1997, ''Experimental Investigation of Flow Through an Asymmetric Planar Diffuser,'' Report TSD-107, Department of Mechanical Engineering, Stanford University, Stanford, CA.

[4] Westphal, R. V., Eaton, J. K., and Johnston, J. P., 1981, ''A New Probe for Measurement of Velocity and Wall Shear Stress in Unsteady, Reversing Flow,'' ASME J. Fluids Eng., **103**, pp. 478–482.

[5] Hussain, A. K. M. F., and Reynolds, W. C., 1970, ''The Mechanics of a Perturbation Wave in Turbulent Shear Flow,'' Report FM-6, Department of Mechanical Engineering, Stanford University, Stanford, CA.

[6] Buice, C. U., and Eaton, J. K., 1999, ''Turbulent Heat Transport in a Perturbed Channel Flow,'' ASME J. Heat Transfer, **199**, pp. 322–325.


# Couette Flow Profiles for Two Nonclassical Taylor-Couette Cells


**Michael C. Wendl**
Postdoctoral Research Associate, School of Medicine, Washington University, Saint Louis, MO 63108

**Ramesh K. Agarwal**
Bloomfield Distinguished Professor and Executive Director, National Institute for Aviation Research, Wichita, KS 67260



*Exact solutions for the Couette profile in two nonclassical Taylor-Couette cells are reported. The profiles take the form of eigenfunction expansions, whose convergence rates can be significantly accelerated using a representative convergence acceleration algorithm. Results are thus suitable as initial conditions for high resolution numerical simulations of transition phenomena in these configurations.* [S0098-2202(00)02602-X]


## 1 Introduction

Laminar flow transition modes are frequently studied using a Taylor-Couette cell, which consists of a cylindrical stator and rotor with fixed endwalls to confine the fluid. Numerical investigations typically use either Taylor's velocity profile (Taylor [1]) or the linear ''thin gap'' profile (Panton [2]) as an initial condition, perturbing it appropriately to examine the disturbance behavior (Criminale et al. [3], Hua et al. [4], Kedia et al. [5]). Both of these profiles are one-dimensional, neglecting spanwise variations such as end effects from the stator walls. While suitable for the theoretical case of infinite span, they are inappropriate for a number of practical situations, e.g., for cells whose span and gap dimensions are of the same order and for the so-called ''nonclassical'' cells whose gap dimension varies along the span (Wiener et al. [6]). Both of these types of cells generally exhibit significant spanwise dependencies. Moreover, variation in nonclassical cells can extend to the boundary, for example when the rotor radius is not constant.

The focus of this note is on deriving Couette flow profiles for two specific nonclassical configurations of current interest, a coni-


Contributed by the Fluids Engineering Division of THE AMERICAN SOCIETY OF MECHANICAL ENGINEERS. Manuscript received by the Fluids Engineering Division July 8, 1999; revised manuscript received February 7, 2000. Associate Technical Editor: M. R. Hajj.

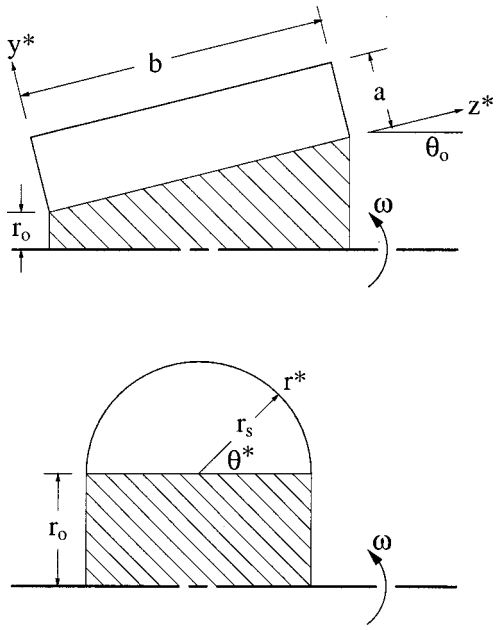


**Fig. 1 Schematic of the conical cell (top) and the spanwise convex stator cell (bottom). Cross-hatched areas represent the rotor and the remaining line segments denote the stator. Cells are symmetric about the center line and the star notation indicates dimensional coordinates.**

cal cell and a cell whose stator is convex along its span. Conical cells (Fig. 1(top)) have been used to examine supercritical flow modes, both experimentally (Wimmer [7–9]) and numerically (Abboud [10]), but transition modes have not yet been extensively studied. Results for convex stator geometries are currently limited to the idealized model of small convexity and infinite span (Eagles and Eames [11]). Although the standard Taylor profile can be conveniently adapted to this case, it is not an experimentally relevant configuration because of the assumption of infinite span. Therefore, the case of a semi-circular cross section is addressed (Fig. 1(bottom)) in this paper. This geometry exhibits both a finite span and significant convexity relative to the span. Exact solutions for the Couette profile for these two configurations do not appear in the literature (Carslaw and Jaeger [12], Berker [13], Wang [14]). The present approach employs, an integral transform method (Ölçer [15]) to obtain exact solutions as expansions in characteristic eigenfunctions. Convergence properties of these expansions, which determine their suitability for use in a numerical solver, are evaluated by applying a representative convergence acceleration algorithm (Brezinski [16], Singh and Singh [17]).

## 2 Analytical Solutions

Wimmer's experimental results on nonclassical cells (Wimmer [9]) suggest that the Couette mode cannot be physically sustained when curvature effects are significant. The fundamental flow mode is fully three-dimensional under such conditions. Consequently, geometries are presently restricted to small curvature effects; the gap dimension is assumed small compared to the rotor radius and the taper is also assumed small. As a result, curvature terms vanish and the Navier-Stokes equations reduce to Laplace's equation for the dimensionless azimuthal velocity component $u$ (Wang [14]),

$$\nabla^2 u = 0. \tag{1}$$

For the conical cell model (Fig. 1($a$)), gap width and cell span are $a$ and $b$, respectively, the cone angle is $0 \leqslant \theta_0 \leqslant \pi/2$, the reference radius is $r_0 > 0$, and the Laplacian operator $\nabla^2$ in Cartesian $(x,y)$ coordinates is $\partial^2/\partial y^2 + \partial^2/\partial z^2$. Dimensional analysis yields three geometric parameters: the aspect ratio $\phi = b/a$, the radius ratio $R = r_0/a$, and the taper factor $T = b \sin\theta_0/r_0$, which is taken as a measure of taper effects. Wimmer's restriction [9] dictates that $R^{-1}$ and $T$ should be small. Using $a$ and $a\omega$ as length and velocity scales, respectively (where $\omega$ is the rotor's rotation rate), the nondimensional boundary conditions are

$$u = 0 \quad at \quad z = 0, \; z = \phi, \quad and \quad y = 1, \tag{2a}$$

and

$$u = R + z \sin\theta_0 \quad at \quad y = 0. \tag{2b}$$

An appropriate integral transform pair is given by

$$\overline{u}(y,\beta_m) = \int_0^{\phi} Z(\beta_m, z')\, u(y,z')\, dz' \tag{3a}$$

and

$$u(y,z) = \sum_{m=1}^{\infty} \frac{Z(\beta_m, z)\,\overline{u}(y,\beta_m)}{\displaystyle\int_0^{\phi} Z^2(\beta_m, z')\, dz'}. \tag{3b}$$

The overbar notation represents a transform in the $z$ coordinate direction, $\beta_m$ are the corresponding eigenvalues, and $Z(\beta_m, z)$ are the corresponding eigenfunctions. All eigen-related quantities can be obtained from standard tables (Özişik [18]).

Applying transform (3$a$) to Eqs. (1), (2$a$), and (2$b$) yields the auxiliary equation $\overline{u}'' - \beta_m^2 \overline{u} = 0$, and two auxiliary boundary conditions $\overline{u} = 0$ at $y = 1$ and $\overline{u} = \phi R([1-(-1)^m] - T[-1]^m)/m\pi$ at $y = 0$. A Sturm-Liouville equation and integration by parts have been used to evaluate various terms. The solution of this system is

$$\overline{u} = \frac{\phi R([1-(-1)^m] - T[-1]^m)\sinh m\pi(1-y)/\phi}{m\pi \sinh m\pi/\phi}. \tag{4}$$

Inverse transform (3$b$) is applied to Eq. (4) to obtain the physical profile in $(y,z)$ space. After eliminating all noncontributing modes, the final result is found to be

$$u(y,z) = \frac{2R}{\pi} \sum_{m=1}^{\infty} \left( \frac{2 \sinh \dfrac{(2m-1)\pi(1-y)}{\phi} \sin \dfrac{(2m-1)\pi z}{\phi}}{(2m-1)\sinh \dfrac{(2m-1)\pi}{\phi}} - \frac{T[-1]^m \sinh \dfrac{m\pi(1-y)}{\phi} \sin \dfrac{m\pi z}{\phi}}{m \sinh \dfrac{m\pi}{\phi}} \right). \tag{5}$$

It is readily apparent that for vanishing taper, $T \to 0$, Berker's two-dimensional thin-gap solution (Berker [13]) for the classical case is recovered.

The convex stator configuration in Fig. 1(bottom) is characterized by $R$, which is the radius of the rotor $r_0$, divided by the radius of the stator's cross section $r_s$. Since the endwalls are effectively formed by the stator itself, there is no separate characterization of the aspect ratio. Moreover, $r_s$ describes the convexity which is a fixed ratio of 1:2 relative to the span of $2r_s$. The curvature restriction again suggests that $R$ must be large. The Laplacian operator in Eq. (1) is now expressed in cylindrical $(r,\theta)$ coordinates as $(1/r)\partial/\partial r(r\,\partial/\partial r) + (1/r^2)\partial^2/\partial\theta^2$. After nondimensionalization, boundary conditions can be expressed as

$$u = R \quad at \quad \theta = 0 \quad and \quad \theta = \pi, \tag{6a}$$

and

$$u = 0 \quad at \quad r = 1. \tag{6b}$$

An appropriate integral transform pair is given by

$$\overline{u}(r,m)=\int_0^{\pi}\Theta(m,\theta')u(r,\theta')d\theta' \tag{7a}$$

and

$$u(r,\theta)=\sum_{m=1}^{\infty}\frac{\Theta(m,\theta)\overline{u}(r,m)}{\int_0^{\pi}\Theta^2(m,\theta')d\theta'}, \tag{7b}$$

where eigenvalues and eigenfunctions are denoted respectively by $m$ and $\Theta(m,\theta)$. Because the domain of $\theta$ is $0\leqslant\theta\leqslant\pi$, this configuration is a special case in which the $\theta$ eigenvalues are integers, as indicated by Eq. (7*b*).

Transformation using Eq. (7*a*) yields $\overline{u}''+\overline{u}'/r-(m/r)^2\overline{u}+mR(1-\cos m\pi)/r^2=0$, a nonhomogeneous equation of the Euler-Cauchy type, and the boundary condition $\overline{u}=0$ at $r=1$. An auxiliary boundary condition $\overline{u}=$*finite* at $r=0$ is also available. By substituting $\overline{u}(r,m)=\overline{\psi}(r,m)+R(1-\cos m\pi)/m$, the homogeneous form of the equation for $\overline{\psi}$ is obtained and is solved with standard methods. The auxiliary solution is then obtained as

$$\overline{u}=\frac{R[(-1)^m-1](r^m-1)}{m}. \tag{8}$$

Inverting Eq. (8) using Eq. (7*b*), the physical solution in $(r,\theta)$ space is found after simplification to be

$$u(r,\theta)=R\left(1-\frac{4}{\pi}\sum_{m=1}^{\infty}\frac{r^{2m-1}\sin(2m-1)\theta}{(2m-1)}\right). \tag{9}$$

## 3 Numerical Evaluation of Series

Use of Eqs. (5) and (9) as initial profiles for numerical computations requires evaluating these expressions for each finite-volume in a computational grid. Processing effort increases not only with grid resolution, but is also dramatically affected in regions where convergence slows considerably. Brezinski's three step acceleration algorithm (Brezinski [16], Singh and Singh [17]) is applied to determine whether the number of terms required for convergence in such regions can be reduced to a manageable level. Taking $S_m$ as the partial sum of $m$ terms such that $S_m\rightarrow S$ as $m\rightarrow\infty$, where $S$ is the complete summation, the two preliminary steps in the algorithm are $\Gamma_1^m=S_m$ and $\Gamma_2^m=(\Gamma_1^{m+1}-\Gamma_1^m)^{-1}$. Progressive estimates of $S$ are given by the third step

$$\Gamma_3^m=\Gamma_1^{m+1}+\frac{(\Gamma_1^{m+2}-\Gamma_1^{m+1})(\Gamma_2^{m+2}-\Gamma_2^{m+1})}{\Gamma_2^{m+2}-2\Gamma_2^{m+1}+\Gamma_2^m}. \tag{10}$$

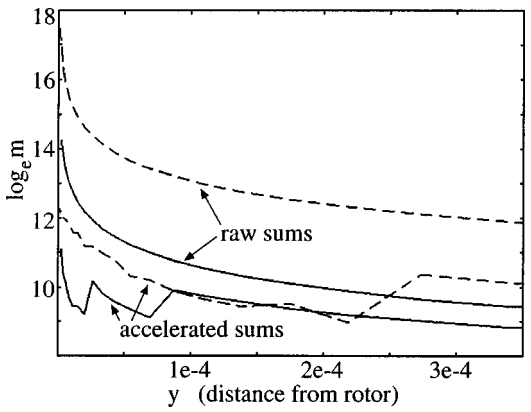


**Fig. 2 Convergence properties of raw and accelerated series at $z=\phi/2$ in the conical cell; $\phi=1$, ——; $\phi=12.75$, — — —. The abscissa and ordinate show nondimensional distance from the rotor and $\log_e$ of the number of terms required for convergence, respectively.**

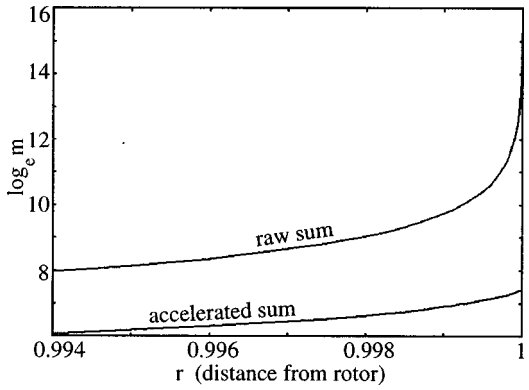


**Fig. 3 Convergence properties of raw and accelerated series at $\theta=\pi/2$ in the convex stator cell. Axes are the same as for Fig. 2.**

Convergence properties are examined for each cell at the center of their spans, i.e., at $z=\phi/2$ for the conical cell and $\theta=\pi/2$ for the convex cell. At the boundaries, the nondimensional grid size is taken to be of order $\delta=10^{-6}$ and is allowed to stretch at the rate of 25 percent toward the interior of the cross section. Convergence is considered achieved when double-precision accuracy has been attained.

Convergence properties of Eq. (5) are independent of $R$ since it appears outside the summation. Moreover, $T$ does not affect convergence for values in the range of physical interest, i.e., $0.01\leqslant T\leqslant 0.1$. The cell aspect ratio is thus the only important parameter. Two values are examined, $\phi=1$ for a square cross section and $\phi=12.75$, which corresponds to Wimmer's experimental configuration [9]. Convergence for both cases requires about $10^1$ terms in the series near the stator and approximately $10^3$ and $10^4$ terms, respectively, for $\phi=1$ and $\phi=12.75$ at $y\sim 0.001$. These results can be considered acceptable for a coarse grid whose smallest volume is $\sim 10^{-3}$. However, for finer grids convergence slows considerably nearer to the rotor. Figure 2 shows results for $y<0.0003$; Brezinski's algorithm yields significant acceleration in this region. At $y\sim 10^{-6}$, the raw series for $\phi=1$, which requires approximately $10^6$ terms for convergence, is accelerated by a factor of about 30. For $\phi=12.75$, the raw series requires on the order of $10^7$ terms, while the accelerated series converges about 180 times faster.

Like the conical cell, convergence in much of the convex stator cross section ($r<0.99$) is reasonably good, requiring approximately $10^1$ to $10^3$ terms. However, convergence degrades rapidly for the remaining 1 percent of the cell near the stator (Fig. 3), requiring $10^7$ terms for $r\sim 1-10^{-6}$. In this case, the Brezinski algorithm results in an acceleration factor of $10^4$. The better performance for this configuration is due to the fact that Eq. (9) is monotonic, whereas Eq. (5) has alternating terms.

## 4 Conclusion

Exact series solutions for Couette flow profiles in two nonclassical geometries of current experimental interest are reported. Convergence of these series is shown to be improved significantly using a representative convergence acceleration algorithm. These results can therefore be effectively used as initial conditions for high-resolution numerical studies of flow transition in these cells.

## References

[1] Taylor, G. I., 1923, ''Stability of a Viscous Liquid Contained Between Two Rotating Cylinders,'' Philos. Trans. R. Soc. London, Ser. A, **223**, pp. 289–343.
[2] Panton, R. L., 1984, *Incompressible Flow*, Wiley, New York.
[3] Criminale, W. O., Jackson, T. L., Lasseigne, D. G., and Joslin, R. D., 1997,

''Perturbation Dynamics in Viscous Channel Flows,'' J. Fluid Mech., **339**, pp. 55–77.
[4] Hua, B. L., Gentil, S. L., and Orlandi, P., 1997, ''First Transitions in Circular Couette Flow with Axial Stratification,'' Phys. Fluids, **9**, pp. 365–375.
[5] Kedia, R., Hunt, M. L., and Colonius, T., 1998, ''Numerical Simulations of Heat Transfer in Taylor-Couette Flow,'' ASME J. Heat Transfer, **120**, pp. 65–71.
[6] Wiener, R. J., Snyder, G. L., Prange, M. P., Frediani, D., and Diaz, P. R., 1997, ''Period-Doubling Cascade to Chaotic Phase Dynamics in Taylor Vortex Flow with Hourglass Geometry,'' Phys. Rev. E, **55**, pp. 5489–5497.
[7] Wimmer, M., 1985, ''Einfluß der Geometrie auf Taylor-Wirbel,'' Z. Angew. Math. Mech., **65**, pp. T255–T256.
[8] Wimmer, M., 1988, ''Viscous Flows and Instabilities Near Rotating Bodies,'' Prog. Aerosp. Sci., **25**, pp. 43–103.
[9] Wimmer, M., 1995, ''An Experimental Investigation of Taylor Vortex Flow Between Conical Cylinders,'' J. Fluid Mech., **292**, pp. 205–227.
[10] Abboud, M., 1988, ''Ein Beitrag zur theoretischen Untersuchung von Taylor-Wirbeln im Spalt zwischen Zylinder/Kegel-Konfigurationen,'' Z. Angew. Math. Mech., **68**, pp. T275–T277.
[11] Eagles, P. M., and Eames, K., 1983, ''Taylor Vortices Between Almost Cylindrical Boundaries,'' J. Eng. Math., **17**, pp. 263–280.
[12] Carslaw, H. S., and Jaeger, J. C., 1959, *Conduction of Heat in Solids*, Clarendon Press, Oxford.
[13] Berker, R., 1963, ''Intégration des équations du mouvement d'un fluide visqueux incompressible,'' *Handbuch der Physik*, (Flügge, S.), VIII/2, Berlin, Springer-Verlag.
[14] Wang, C. Y., 1991, ''Exact Solutions of the Steady-State Navier-Stokes Equations,'' Annu. Rev. Fluid Mech., **23**, pp. 159–177.
[15] Ölçer, N. Y., 1964, ''On the Theory of Conductive Heat Transfer in Finite Regions,'' Int. J. Heat Mass Transf., **7**, pp. 307–314.
[16] Brezinski, C., 1982, ''Some New Convergence Acceleration Methods,'' Math. Comput., **39**, pp. 133–145.
[17] Singh, S., and Singh, R., 1993, ''Use of Linear and Nonlinear Algorithms in the Acceleration of Doubly Infinite Green's Function Series,'' IEE-Proc. H, **140**, pp. 452–454.
[18] Özişik, M. N., 1980, *Heat Conduction*, Wiley, New York.

# A Method for Validating Two-Dimensional Flow Configurations in Particle Streak Velocimetry

**Y. M. Gbamelé**
PhD Student

**P. Desevaux**
Assistant Professor

**J.-P. Prenel**
Professor

Institut de Génie Energétique, Université de Franche-Comté, 2, avenue Jean Moulin, F-90000, Belfort, France

*A polychromatic flow visualization technique for Particle Streak Velocimetry (PSV) is described. The method uses several adjoining laser light sheets of different wavelengths with a homogeneous power density distribution. This method allows us to make sure of the 2-D and 3-D nature of flows and to improve the frames quality processed in PSV. The feasibility study of this qualitative technique is established on a hydrodynamic flow.*
[S0098-2202(00)02402-0]

Contributed by the Fluids Engineering Division of THE AMERICAN SOCIETY OF MECHANICAL ENGINEERS. Manuscript received by the Fluids Engineering Division April 28, 1999; revised manuscript received February 16, 2000. Associate Technical Editor: S. Banerjee.

## 1 Introduction

The methods of velocity measurement by PIV, PTV, PSV have made progress these last years (Grant [1]). Large efforts have focused on the application of these techniques to the study of three-dimensional flow (Hinsch [2]). Unfortunately, the methods proposed are often heavy and complex to implement. So, before using such techniques, it is better to confirm the 2-D or 3-D nature of flows. We present here a qualitative technique based on the polychromatic laser tomography (Prenel et al. [3]) to dispel this ambiguity. The images obtained by this technique allow us to make sure of the 2-D or 3-D nature and can be directly processed in PSV to extract the velocity fields.

## 2 Optical Device

The optical setup (Fig. 1) used to realize three polychromatic laser sheets is taken from the device designed by Prenel et al. [4]. The light source is an argon-krypton laser (Spectra-Physics Laser Stabilite 2017) emitting in all lines with a power of about 4 W. The objective is to obtain parallel sheets with a homogeneous power density distribution and adjustable thickness and width (Prenel and Thiery [5]). This requires two fast horizontal and vertical simultaneous sweepings of the laser beam. So, the device is made up of a first telescope ($T_1$) which focuses the polychromatic beam at the entrance of an Acousto-Optical Deflector (AOD: AA.DTS.X-250, optical range 360–1100 nm). The AOD induces a horizontal sweeping of the beam. The triangular shape of the driving signal guarantees the homogeneity of the power density distribution along the sheet thickness and the amplitude controls its size. The telescope ($T_2$) focuses the beam in the zone of visualization. The Prism with Direct Vision (PDV) disperses the light and the three intense lines (red 647.1 nm, green 514.5 nm, and blue 488 nm) are carried back on three mirrors ($M_1$, $M_2$, and $M_3$). These mirrors restore the beams parallel and three prisms ($P_1$, $P_2$, and $P_3$) enable the space between the polychromatic beams to be adjusted.

The scanning mirror (SM) produces a vertical deviation of the

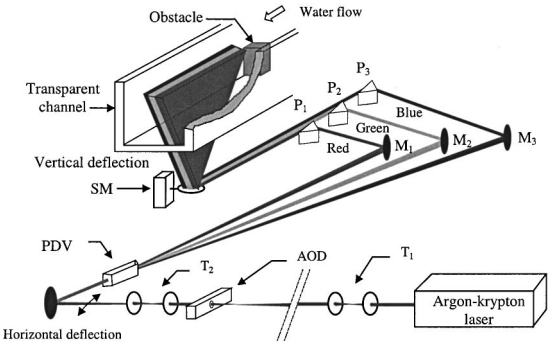


**Fig. 1 Optical device**

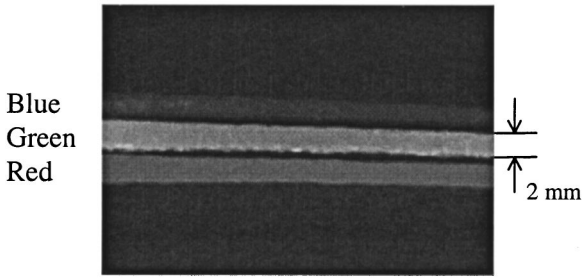


**Fig. 2 Laser sheets dimensions**

  

beams and guarantees the power density homogeneity along the sheets width. The scanning mirror amplitude sets the sheets width dimension.

For a long working distance and a weak sweeping angle, the polychromatic sheets become real parallelepipeds of light with a nearly homogeneous power density.

Figure 2 is a top view photography of the three adjoining laser light sheets. The sheets thickness (equal to 2 mm in the present picture) is the same for the three laser sheets and may be adjusted to values from 0.5 mm to 10 mm.

## 3 Practicability Experiment

The practicability of the method is established on a hydrodynamic flow generated in a transparent channel with a rectangular section (10 cm×4 cm). An obstacle (i.e., a 3 cm×1.5 cm vertical plate) is placed in the hydrodynamic channel (as shown in Fig. 3) in order to disturb the flow and to create 3-D effects. During the tests, the water flows out with an average velocity between 0.05 and 0.25 $ms^{-1}$ corresponding to Reynolds numbers (relative to the hydraulic diameter of the water channel) varying from 3000 to 15,000. The water seeding is performed by means of rilsan spherical particles (Elf Atochem, weak size dispersion around 30 $\mu$m, volumic mass of 1.06 $g/cm^3$). The three light sheets illuminate three parallel planes along the principal flow direction. The flow is observed perpendicularly to the laser sheets by using a 3-CCD color video camera (Sony XC-003P). The images are digitized and stored as 715×535 pixels by an imaging technologies frame buffer board (MiroVideo). The observation field is limited to a rectangular area of 35 mm×25 mm. The three zones of the hydrodynamic channel, which are investigated during this feasibility study, are indicated in Fig. 3.

Figure 4 shows flow visualizations obtained by using the present technique. The exposure time used in the images presented is 1/25 s. When a particle moves in the studied zone, the luminous dash marking its trajectory during the acquisition time presents a uniform contrast due to the homogeneous power distribution within the light volumes. Consequently, the dynamic behavior of the particle can easily be quantified. It can be noticed that a single particle is about 6–7 pixels large. Moreover, the particle streak will be made up of one or several colors according to its displacement.

In 2-D flows parallel to the three sheets, the particles scatter in only one color (i.e., red, green, or blue color). These conditions are those of the initial flow upstream of the obstacle (zone 1) where the flow is expected to be strictly 2-D. This is confirmed by the flow visualization presented in Fig. 4(a) which reveals the presence of particle streaks made up of one color only. This picture shows that the flow remains strictly parallel to the plane illuminated by the laser light sheets. Such conditions are ideal for a classical study by PSV and the 2-D velocity field may be directly determined from such an image.

The photography displayed in Fig. 4(b) is related to the zone 3 located at a long distance (about 40 cm) behind the obstacle. We cannot a priori be sure of the 2-D or 3-D configuration of the flow in this region of the hydrodynamic channel. The flow visualizations performed by the present method clear up the ambiguity relating to the flow pattern and indicate the weak 3-D nature of the flow in this zone. Indeed, we can note the presence of few bicolor or tricolor streaks revealing the 3-D trajectories of some tracers. If these polychromatic streaks are in a small number, the flow may be studied in PSV as a 2-D flow. An image processing procedure may be applied to remove these few polychromatic streaks before extracting the 2-D velocity field.

For highly 3-D flows, the majority of the particle streaks will be made up of 2 or 3 colors. This is illustrated in Fig. 4(c) by the flow visualization performed in the immediate wake of the obstacle (zone 2).

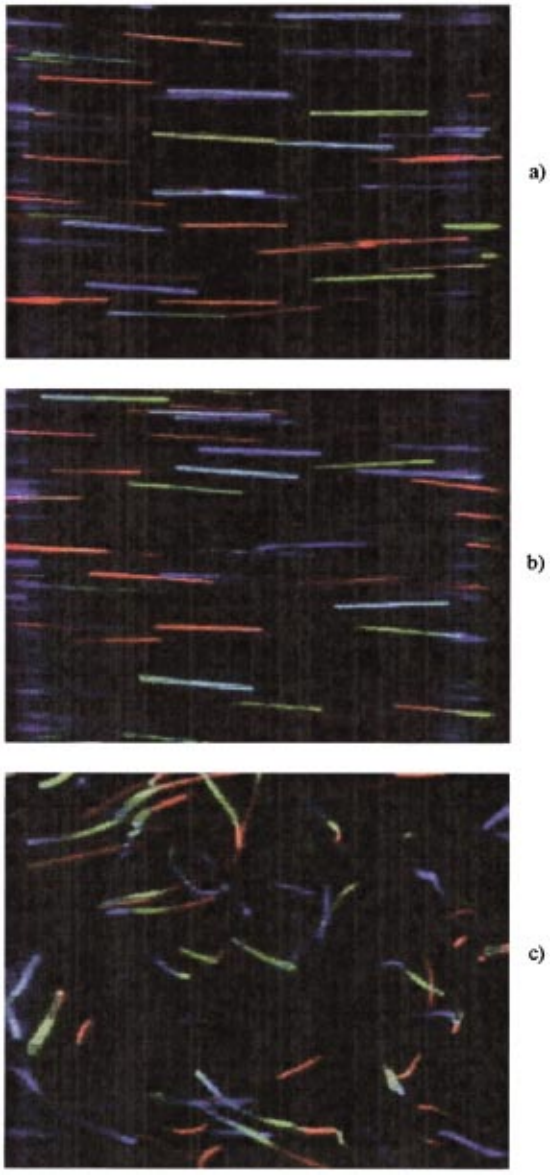


**Fig. 4 (*a*) Strictly 2-D flow; (*b*) weakly 3-D flow; (*c*) highly 3-D flow**

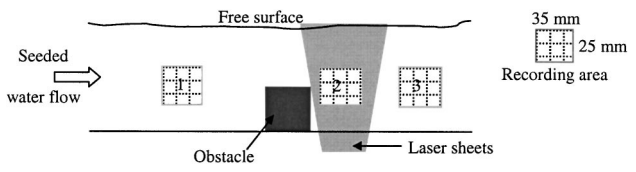


**Fig. 3 Location of the investigated zones (side view of the hydrodynamic channel)**

## 4 Concluding Remarks

A number of conclusions are offered relative to the flow visualization method developed in this paper:

1 The use of polychromatic laser tomography is a simple and efficient way for validating 2-D flow configurations.

2 For weakly 3-D flows, an image processing procedure may be applied to remove polychromatic streaks before extracting the two-dimensional velocity vectors.

3 The present method is illustrated by its application to a hydrodynamic-channel flow but may be extended to gas flows.

4 Limitations of the method depend mainly on the viewing system characteristics: the depth of field of the viewing system limits the laser sheets thickness, the camera sensitivity is not the same for all the wavelengths and consequently an adjustment of the wave lines intensities of the argon-krypton laser is required, and the exposure time of the viewing system must be long enough with respect to the flow velocity so that tracers having possibly 3-D trajectories may cross the three laser sheets in the thickness direction.

5 For very low velocity flows, the thickness of the laser sheets has to be reduced to its minimum value (0.5 mm with the present optical device) in order to enhance the sensitivity of the system to detect possible 3-D effects.

## References


[1] Grant, I., 1997, ''Particle Image Velocimetry: A Review,'' Proc. Inst. Mech. Eng., Part C: J. Mech. Eng. Sci., **211**, pp. 55–76.

[2] Hinsch, K. D., 1995, ''Three-Dimensional Particle Velocimetry,'' Meas. Sci. Technol., **6**, pp. 742–753.

[3] Prenel, J. P., Porcar, R., Polidori, G., Texier, A., and Coutanceau, M., 1992, ''Wavelength Coding Laser Tomography for Flow Visualizations,'' Opt. Commun., **91**, pp. 29–33.

[4] Prenel, J. P., Thiery, L., and Marconot, B., 1997, ''Visualisation par volumes de lumière polychromatique à densité puissance homogène,'' *Proceedings du 7éme Colloque National de Visualisation et de Traitement d'Images en Mécanique des Fluides*, Saint-Louis, France, pp. 35–40.

[5] Prenel, J. P., and Thiery, L., 1997, ''Theoretical Study and Realization of Laser Light Sheets With a 3D Homogeneous Power Density and Controlled Geometrical Parameters,'' *Proceedings of the 1st Pacific Symposium on Flow Visualization and Image Processing*, Honolulu, Hawaii, pp. 537–541.


# Analysis and Validation of One-Dimensional Models for Gaseous Flows in Micro-Channels


**Hongwei Sun**
Research Associate

**Mohammad Faghri**
Professor

Department of Mechanical Engineering and Applied Mechanics, University of Rhode Island, Kingston, RI 02881



*The paper presents three one-dimensional models to simulate gaseous flows in micro-channels. These include no-slip flow, simple fully-developed, and locally fully-developed models. It is shown that the locally fully-developed model provides a more accurate prediction when both rarefaction and gas acceleration need to be considered in micro-flows. Furthermore, the effects of rarefaction and gas acceleration on the locally dimensionless pressure ratio are specified on the basis of the three models. The validation of these models is accomplished by comparison with the experimental results.* [S0098-2202(00)02502-5]



Contributed by the Fluids Engineering Division of THE AMERICAN SOCIETY OF MECHANICAL ENGINEERS. Manuscript received by the Fluids Engineering Division December 9, 1998; revised manuscript received February 14, 2000. Associate Technical Editor: M. S. Cramer.


## Introduction

For gaseous flows in micro-channels, the effect of rarefaction cannot be negligible because Knudsen numbers (ratio of mean free path to characteristic length) are usually greater than 0.01. Arkilic et al. [1,2] developed an analytical model based on the Navier-Stokes equation with the slip boundary condition to predict isothermal helium flows through a parallel plate channel and validated the model with the experimental results with pressure ratios up to 2.5. Shih et al. [3] validated this model by comparing the model results of mass flow rate and pressure distribution for nitrogen and helium flows through micro-channels with their experimental results. Direct Simulation Monte Carlo (DSMC) investigation by Piekos and Breuer [4] showed a discrepancy for pressure distribution when compared with the slip-flow model for a pressure ratio of 4.2. Sun et al. [5] investigated effects of velocity slip and temperature jump on the momentum and heat transport in micro-channels based on locally fully-developed assumption which was used by van den Berg [6] to analyze the compressible isothermal flows in capillaries.

The motivation of this work is to include the acceleration term in the conservation of momentum for a one-dimensional compressible flow model and to find out the relationship among the available one-dimensional models. Furthermore, the effects of rarefaction and gas acceleration on pressure distribution and mass flow rate are related to Re, Ma, and Kn based on the dimensional analysis for the simple fully-developed model and the locally fully-developed model.

## One-Dimensional Models

For a laminar, constant-viscosity, fluid flow in a parallel plate channel, the conservation of axial momentum for an infinitesimal control volume with length $dx$ can be expressed as:

$$-2hdP-2\overline{\tau}_w dx=d\left[\int_{-h}^{h}\rho u^2 dy\right] \tag{1}$$

where $h$ is the half-depth of the channel and $\overline{\tau_w}$ refers to the average shear stress at the wall. DSMC simulation for gaseous flows in micro-channels shows that the maximum ratio of $v(x,y)/u(x,y)$ is less than one percent. Therefore, $P$ can be assumed to be only a function of $x$.

**Locally Fully-Developed Flow Model.** High-pressure drops over relatively short lengths are common in gaseous flows through micro-channels. As a result, density and velocity continually change along the flow axis, and the flow cannot become fully developed. Therefore, a locally fully-developed model is introduced. In this model, the parabolic velocity profile and the wall shear stress are obtained from the fully developed condition and are locally applied at any cross-section along the micro-channel. In other words, the velocity profile $u$ and the average wall shear stress $\overline{\tau_w}$ in Eq. (1) can be obtained from the Navier-Stokes equation with the slip boundary condition for fully developed flows as follows (Shih et al. [3]):

$$u(y)=\frac{h^2}{2\mu}\left(-\frac{dp}{dx}\right)\left[1.0+4\,\frac{2-\sigma_\gamma}{\sigma_\gamma}\mathrm{Kn}-\left(\frac{y}{h}\right)^2\right] \tag{2}$$

$$\overline{\tau}_w=-\mu\left.\frac{du}{dy}\right|_{y=h}=\frac{3}{4}\,\frac{\mathrm{Re}\,\mu^2}{\rho h^2\left(1+6\,\dfrac{2-\sigma_\gamma}{\sigma_\gamma}\mathrm{Kn}\right)} \tag{3}$$

where $\mathrm{Re}=\rho\overline{u}(4h)/\mu$, $\mathrm{Kn}=\lambda/(2h)$ and $\sigma_\gamma$ represents the tangential momentum accommodation coefficient (TMAC) which depends on the gas species, surface characteristics and is usually close to unity.

By substituting Eqs. (2) and (3) into Eq. (1) and integrating along the $x$-direction using the ideal gas law and the continuity equation, an expression for the axial pressure distribution $P$ can be obtained as follows:

$$\left(\frac{P}{P_{in}}\right)^2 - 1.0 + 12\,\mathrm{Kn}_{in}\left(\frac{P}{P_{in}} - 1.0\right) + 2\,\mathrm{Re}^2\,\alpha\beta\left[6\,\mathrm{Kn}_{in}\left(\frac{P_{in}}{P} - 1.0\right) - Ln\left(\frac{P}{P_{in}}\right)\right] = -24\,\mathrm{Re}\,\beta\frac{x}{h} \tag{4}$$

where $\beta$ and $\alpha$ are given by:

$$\beta = \frac{\mu^2 RT}{(4hP_{in})^2}$$

$$\alpha = \frac{9}{4}\frac{\frac{8}{15} + \frac{16}{3}\overline{\mathrm{Kn}} + 16\,\overline{\mathrm{Kn}^2}}{(1 + 6\,\overline{\mathrm{Kn}})^2} \tag{5}$$

$\overline{\mathrm{Kn}}$ is the average Knudsen number along the channel. From Eq. (4), the corresponding mass flow rate can be obtained as follows:

$$G = \frac{h^3 w}{3RTL\mu}P_{out}^2\left[(P^*)^2 - 1.0 + 12\,\mathrm{Kn}_{out}(P^* - 1.0) - 2\left(\frac{\rho\overline{u}}{P_{out}}\right)^2 RT\alpha[6\,\mathrm{Kn}_{in}(P^* - 1.0) + Ln(P^*)]\right] \tag{6}$$

To the author's knowledge, Eqs. (4) and (6) for $P$ and $G$ are presented for the first time here.

**Simple Fully-Developed Model.** By neglecting the axial momentum change in Eq. (1) and using Eq. (3), the axial pressure distribution and mass flow rate can be obtained as follows:

$$\left(\frac{P}{P_{in}}\right)^2 - 1.0 + 12\,\mathrm{Kn}_{in}\left(\frac{P}{P_{in}} - 1.0\right) = -24\,\mathrm{Re}\,\beta\frac{x}{h} \tag{7}$$

$$G = \frac{Wh^3}{3RTL\mu}P_{out}^2[(P^*)^2 - 1.0 + 12\,\mathrm{Kn}_{out}(P^* - 1.0)] \tag{8}$$

Equations (7) and (8) are similar to the slip-flow model developed by Arkilic et al. [2] and Shih et al. [3] and are referred to as ''simple fully-developed model'' in this paper. The simple fully-developed model can predict the increase in mass flow rate due to gas rarefaction in flows through micro-channels.

**Continuum Flow Model.** By setting Knudsen numbers in Eqs. (7) and (8) to zero, the axial pressure distribution and the mass flow rate for the continuum flows can be obtained as:

$$\left(\frac{P}{P_{in}}\right)^2 - 1.0 = -24\,\mathrm{Re}\,\beta\frac{x}{h} \tag{9}$$

$$G = \frac{Wh^3}{3RTL\mu}P_{out}^2[(P^*)^2 - 1.0] \tag{10}$$

Comparison of Eqs. (8) and (10) shows that slip-flow causes an increase in mass flow rate for a given inlet and outlet pressures. However, according to Eq. (6), an increase in mass flow rate is reduced by gas acceleration for high pressure flow conditions. The following analysis reveals that the effect of the gas acceleration can be related to Mach number (Ma) in micro-flows when an isothermal assumption is valid.

## Discussion and Validation

**Pressure Distribution.** Rarefaction and compressibility effects on gaseous flows in micro-channels have been studied by Beskok et al. [7] using numerical simulation for two-dimensional flows with a second-order slip boundary condition. However, for the first time in this paper, the relationships between the local pressure variation and the parameters Kn, Re, and Ma are shown based on the dimensional analysis for one-dimensional models.

For compressible no-slip flows, the axial $\mathbf{p}^2$ gradient can be obtained by differentiating Eq. (9) with respect to $x$ as:

$$\left(\frac{dP^2}{dx}\right)_{\text{continuum}} = -\frac{3}{2}\frac{\mathrm{Re}\,\mu^2 RT}{h^3} \tag{11}$$

From the Eqs. (7) and (4), the corresponding relationships based on the simple fully-developed model and the locally fully-developed model can be obtained as:

$$\left(\frac{dp^2}{dx}\right)_{\text{simple}} = -\frac{3}{2}\frac{\mathrm{Re}\,\mu^2 RT}{h^3(1 + 6\,\mathrm{Kn})} \tag{12}$$

$$\left(\frac{dp^2}{dx}\right)_{\text{local}} = -\frac{3}{2}\frac{\mathrm{Re}\,\mu^2 RT}{h^3(1 + 6\,\mathrm{Kn})(1 - \mathrm{Re}^2\,\mathrm{Kn}^2/2\pi)} \tag{13}$$

where the following definition of Knudsen number is used:

$$\mathrm{Kn} = \frac{\mu\sqrt{\pi RT}}{2\sqrt{2}hp} \tag{14}$$

The subscript **continuum** refers to the compressible no-slip flow model and subscripts **slip** and **local** represent the simple fully-developed flow and the locally fully-developed flow model, respectively.

From Eqs. (11) and (12), it is clear that rarefaction reduces the pressure drop and friction factor. The reduction is quantified by the term $(1 + 6\,\mathrm{Kn})$. However, the negative effect is contributed by the gas acceleration term $(1 - \mathrm{Re}^2\,\mathrm{Kn}^2/2\pi)$ in Eq. (13). This conclusion—compressibility negating rarefaction—was also reached by Beskok et al. [7] based on his numerical simulation.

The Knudsen number can be expressed as a function of Mach number and Reynolds number (Eckert and Drake [8]) as:

$$\mathrm{Kn} = \frac{\lambda}{2h} = \sqrt{\gamma\pi/2}\,\frac{2\,\mathrm{Ma}}{\mathrm{Re}} \tag{15}$$

By using Eq. (15), the term $(1 - \mathrm{Re}^2\,\mathrm{Kn}^2/2\pi)$ in Eq. (13) can be replaced by $(1 - \gamma\,\mathrm{Ma}^2)$ to evaluate the gas acceleration. It is clear that rarefaction and acceleration have opposite effects on pressure variation and the terms $(1 + 6\,\mathrm{Kn})$ and $(1 - \gamma\,\mathrm{Ma}^2)$ represent the effects of slip flow and gas acceleration, respectively.

**Mass Flow Rate.** Comparison of mass flow rate versus pressure ratios between the three models and the experiment by Arkilic [1] is shown in Fig. 1. The experiment was conducted in a $52.25\,\mu\mathrm{m} \times 1.33\,\mu\mathrm{m} \times 7500\,\mu\mathrm{m}$ micro-channel using nitrogen as the working fluid. It was found that rarefaction has an important

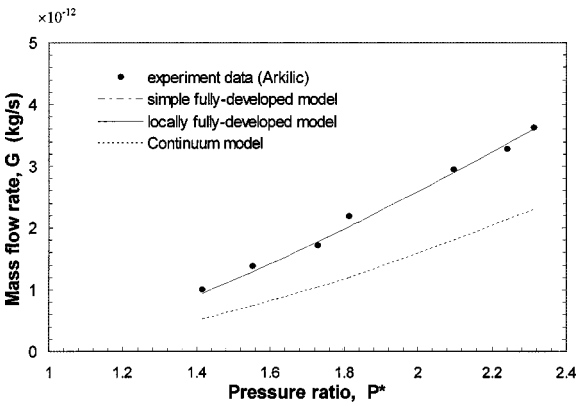


**Fig. 1 Comparison of experimental results of Arkilic with the simple fully-developed model, the locally fully-developed model, and the continuum flow model**

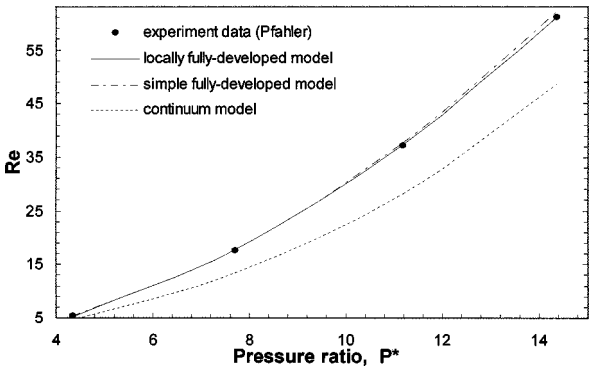


**Fig. 2 Comparison of the experimental results by Pfahler [9] with the prediction from the three models**

**Table 1 Comparison between the terms $(1+6\,\mathrm{Kn})$ and $(1-\gamma\,\mathrm{Ma}^2)$ at the outlet for Pfahler's [9] experiment**

| $P^*$ | $1+6$ Kn | $1-\gamma\,\mathrm{Ma}^2$ |
|---|---|---|
| 4.3 | 1.084 | 0.999 |
| 7.6 | 1.084 | 0.992 |
| 12.1 | 1.084 | 0.954 |
| 14.1 | 1.084 | 0.906 |
| 21.0 | 1.084 | 0.578 |

effect on mass flow rate in the microchannel as was also reported by other researchers. There exists a 17 percent deviation between the results from the continuum flow model and the experiment at the pressure ratio of 2.6 when the Knudsen numbers are 0.062 and 0.165 at the inlet and outlet, respectively. The deviation increases with the increase in pressure ratios. The simple fully-developed model and the local fully-developed model are both in good agreement with the experimental results for pressure ratios below 3.0. Simulation for higher-pressure ratios shows that the deviation between the two models is below 1.0 percent for a pressure ratio of 14.0. The term $\gamma\,\mathrm{Ma}^2$, which represents the effect of gas acceleration, has a magnitude of $10^{-6}$ at a pressure ratio of 2.6 and $10^{-4}$ for a pressure ratio of 14.0 and is still four orders of magnitudes smaller than the term 6 Kn which represents the effect of rarefaction.

Experimental data reported by Pfahler [9] was also employed to check the three models. In this experiment, nitrogen was driven through a $98.73\,\mu\mathrm{m}\times 4.65\,\mu\mathrm{m}\times 10{,}900\,\mu\mathrm{m}$ micro-channel and Reynolds number ranges from 5 to 60 with the fixed outlet Knudsen number of 0.014. Simulation results based on the continuum flow, simple fully-developed flow and local fully-developed flow models are presented in Fig. 2. It can be seen that the locally fully-developed model and the simple fully-developed model accurately predict the mass flow rate when $P^*$ is smaller than 7.6. The deviation appears for higher values of $P^*$. The corresponding variations of the terms $(1+6\,\mathrm{Kn})$ and $(1-\gamma\,\mathrm{Ma}^2)$ are shown in Table 1. When $(1-\gamma\,\mathrm{Ma}^2)$ varies from 0.999 to 0.906 ($P^*$ increase from 4.3 to 14.1), the deviation between the simple fully-developed and locally fully-developed flow models increases from 0.5 percent to 3 percent and become higher with increasing $P^*$ based on the value of the term $(1-\gamma\,\mathrm{Ma}^2)$. Further experimental data for higher-pressure ratios is needed to check the accuracy of the locally fully-developed model in micro-flows.

## Nomenclature

$G$ = mass flow rate, $\rho\bar{u}W(2h)$
$h$ = half-depth of the channel
Kn = Knudsen number, $\lambda/2h$
$L$ = channel length
Ma = Mach number
$P$ = pressure
$P^*$ = inlet to outlet pressure ratio, $P_{\mathrm{in}}/P_{\mathrm{out}}$
$R$ = gas constant
Re = Reynolds number, $\rho\bar{u}(4h)/\mu$
$T$ = temperature
$u$ = velocity in $x$-direction
$\bar{u}$ = average velocity in $x$-direction
$v$ = velocity in $y$-direction
$W$ = channel width
$x,y$ = Cartesian coordinates
$\alpha,\beta$ = constants, Eq. (5)
$\gamma$ = specific heat ratio
$\lambda$ = mean free path
$\mu$ = viscosity
$\rho$ = density
$\tau$ = shear stress
$\sigma_\gamma$ = tangential momentum accommodation coefficient

### Subscripts

continuum = compressible no-slip flow
in = inlet
local = locally fully-developed model
out = outlet
simple = simple fully-developed model
$w$ = wall

## References

[1] Arkilic E. B., Breuer K. S., and Schmidt M. A., 1994, ''Gaseous Flow in Micro-Channels,'' *Applications of Microfabrication to Fluid Mechanics*, ASME, FED-Vol. 197, pp. 57–66.
[2] Arkilic, E. B., Schmidt, M. A., and Breuer, K. S., 1997, ''Gaseous Slip Flow in Long Microchannels,'' J. Microelectromech. Syst., IEEE, **6**, pp. 167–178.
[3] Shih, J. C., Ho, C., Liu, J., and Tai, Y., 1996, ''Monatomic and Polyatomic Gas Flow Through Uniform Microchannels,'' Microelectromechanical Systems (MEMS), ASME, DSC-59, pp. 197–203.
[4] Piekos, E. S., and Breuer, K. S., 1996, ''Numerical Modeling of Micromechanical Devices Using the Direct Simulation Monte Carlo Method,'' ASME J. Fluids Eng., **118**, pp. 464–469.
[5] Sun, H., Gu, W., and Liu, W., 1998, ''Effects of Slip-flow and Temperature-jump on Momentum and Heat Transport in Micro-channels,'' J. Eng. Thermophys., **19**, No. 1, pp. 94–97.
[6] van den Berg, H. R., ten Seldam, C. A., and van der Gulik, P. S., 1993, ''Compressible Laminar Flow in a Capillary,'' J. Fluid Mech., **246**, pp. 1–20.
[7] Beskok, A., Karniadakis, G. E., Trimmer, W., 1996, ''Rarefaction and Compressibility Effects in Gas Microflows,'' ASME J. Fluids Eng., **118**, pp. 448–456.
[8] Eckert, E. R. G., and Drake R. M., 1972, *Analysis of Heat and Mass Transfer*, McGraw-Hill, New York.
[9] Pfahler J., Harley J., Bau H. H., and Zemel J., 1990, ''Liquid and Gas Transport in Small Channels,'' ASME, DSC-19, pp. 149–157.